Microwave Breast Imaging using a Dry Setup

João M. Felício, *Member, IEEE*, José M. Bioucas-Dias, *Fellow, IEEE*, Jorge R. Costa *Senior Member, IEEE*, and Carlos A. Fernandes, *Senior Member, IEEE*

***Abstract*—The paper demonstrates for the first time, both numerically and experimentally, the feasibility of radar-based microwave imaging of anthropomorphic heterogeneously dense breasts in prone position, requiring no immersion liquid. The dry, contactless approach greatly simplifies the setup, favors patient comfort, and further avoids lengthy sanitation procedures after each exam. We use a radar-type technique with the antennas distributed in cylindrical configuration around the breast phantom. The reflectivity map is reconstructed using a wave-migration algorithm in the frequency domain. The paper presents new developed strategies to cope with the challenges of a dry setup, namely increased skin artifact due to the concomitant absence of matching liquid and non-uniform breast shape. We propose an iterative and adaptive algorithm based on singular value decomposition that effectively removes the skin backscattering under the above conditions. It is compatible with automatic processing, and computationally fast. One of its inputs is the breast three-dimensional surface information, and its distance to the antennas, all obtained automatically from a proposed low-cost procedure based on a webcam. The imaging method is reasonably resilient to the presence of fibroglandular tissues, and to uncertainties of tissue permittivity. Another tackled challenge is the miniaturization of the antenna in air, which is achieved with an optimized balanced antipodal Vivaldi of the same size as counterparts used in dense immersion liquids. Finally, all the building blocks are combined to demonstrate experimentally the overall dry system performance, with very good detection of the tumor at three different positions in the breast, even in low contrast scenarios.**

***Index Terms*—artifact removal, balanced antipodal Vivaldi antenna (BAVA), breast surface estimation, broadband antenna, dry imaging setup, heterogeneous breast imaging, inverse problem, medical microwave imaging (MWI), phantom, singular value decomposition (SVD), skin backscattering, cascade transmission line, wave-migration.**

I. Introduction

OVER the last two decades, Microwave Imaging (MWI) has been investigated as an alternative imaging modality for breast cancer screening. *De facto* techniques, such as mammography (X-rays) and Magnetic Resonance Imaging (MRI), have well known limitations [1], which contributed to the emergence of new technologies.

Active MWI systems illuminate the breast with electromagnetic (EM) energy usually comprised in the frequency spectrum between 1 GHz and 10 GHz. The microwave energy is radiated by antennas distributed around the breast. Given the permittivity contrast of different tissues, the EM waves are scattered and picked up by the same or separate antennas [1]. In the specific case of breast cancer detection, MWI benefits from high contrast between healthy and malignant tissues [1].

It is common to categorize MWI methods as quantitative or qualitative. The first type aims at spatially mapping the dielectric properties of media in the frequency-domain, for instance by means of the distorted Born's or Rytov's linear approximation [2], [3]. Quantitative methods involve time-consuming iterative calculations to find the solutions of ill-posed inverse problem, which depends greatly on the accuracy of the forward model and on good initializations [2], [4]. In contrast, qualitative imaging aims at reconstructing the reflectivity of a given volume [5] and is compatible with real-time examinations. In the present work we focus on qualitative techniques based on radar-approach.

Due to the restricted bandwidth and relatively large wavelengths, the attainable resolution of microwaves is of a few centimeters in free-space, which contrasts with the fine resolution of X-rays. Nevertheless, unlike mammography, microwaves do not pose any health risk and are compatible with contactless imaging setup. Moreover, medical MWI is intended as a primary screening examination method and not as the ultimate and single-validation examination. In case of such detection, patients would be forwarded to other exams, such as MRI or ultrasound. We highlight that this is already standard procedure with mammography. The attainable resolution using microwaves is addressed in more detail ahead in this paper.

Given the high permittivity contrast between skin and air, the received signals are dominated by this early-time reflection [6]. This artifact is easily hundreds of times larger in magnitude than the tumor response, which can potentially mask the tumor, thus precluding its detection. Consequently, before addressing the image reconstruction, it is necessary to eliminate (or at least significantly reduce) the early-time response from the skin. This processing step is known as artifact removal.

A typical strategy to mitigate the skin backscattering is to immerse the breast in a coupling medium [7]- [9]. Nevertheless, some researchers have recently explored dry breast imaging setups using computationally heavy tomographic techniques for image inversion [10], [11], or faster holographic techniques [12], [13]. The latter make no reference to the

Manuscript received...

This work was partly funded by Fundação para a Ciência e Tecnologia (FCT) under projects PTDC/EEI-TEL/30323/2017 and under grant SFRH/BD/115671/2016, and by Instituto de Telecomunicações, and Universidade de Lisboa. It was also funded by FCT/MEC through national funds and co-funded by FEDER – PT2020 partnership agreement under project UID/EEA/50008/2019. This work has been developed in the framework of COST Action TD1301 (MiMed).

J. M. Felício and J. R. Costa are with Instituto de Telecomunicações, Instituto Superior Técnico (IT-IST), Universidade de Lisboa, Lisbon 1049-001, Portugal, and also with the Departamento de Ciências e Tecnologias de Informação, Instituto Universitário de Lisboa (ISCTE-IUL), Lisbon 1649-026, Portugal (e-mail: joao.felicio@lx.it.pt).

J. M. Bioucas-Dias and C. A. Fernandes are with Instituto de Telecomunicações, Instituto Superior Técnico (IT-IST), Universidade de Lisboa, Lisbon 1049-001, Portugal.

artifact removal algorithm and enable only two-dimensional images of the breast, whereas [10], [11] use a simplified anatomic structure to model the breast, and benefit from a more favorable contrast between fibroglandular and tumor tissues than what is generally reported in the literature [14]. Also, the papers do not address issues related to the real measurement scenario and experimental setup. In fact, no one has yet fully analyzed the impact of a contactless dry approach [15]. The contact liquid makes the setup much more complex and bulky than a dry one. Moreover, immersing the breast poses sanitation issues, complicates the maintenance of the examination setup, and makes the exam longstanding and somewhat uncomfortable to the patient. Therefore, we investigate whether it is imperative to use a coupling medium. To this end, we assume a transmission line model (TLM) representing each layer of the body plus the external medium, and calculate the corresponding scattering matrix. The dry setup shows some increase of skin backscatter, but, as demonstrated in this paper, not enough to rule it out.

Without the coupling medium, larger efforts are required by the artifact removal algorithm, which relies on a precise retrieval of the breast 3D shape and the antenna distances to the breast skin. This issue has been addressed in [16] and [17]. However, the solutions proposed in those works are either rather expensive [16] or require complex measurement schemes [17]. We propose a technique based on a commercial webcam, which is not only low-cost, but also involves less measurement points. The information is fed into our proposed artifact removal technique, which is based on the Singular Value Decomposition (SVD) factorization [18]. This method decomposes the measured data into a set of reflections, allowing removing the stronger echoes originated by the breast skin. We introduce an automation-compatible iterative procedure that adapts the echo removal algorithm to the reflection information in the measured data, without introducing distortion in the tumor position. The algorithm is fast, and compatible with real-time or near-real-time processing. As discussed in [19], precise breast shape and antenna distance information not only benefit the effectiveness of the artifact removal algorithm but also improves the accuracy of the final tumor image reconstruction. The methods described in this paragraph are key to make dry setups viable. SVD is used in other works as well [8], [20], but using simplistic assumptions such as that of revolution-symmetric phantoms.

The absence of coupling medium no longer benefits the antenna size and the antenna-breast interaction. Therefore, it requires the design of miniaturized broadband antennas compatible with the available volume around the breast. This subject is also one of the goals of the present study.

As an ultimate objective, leveraging all the aforementioned elements, we test experimentally a complete dry MWI system for breast cancer screening in prone position. The advantages of this examination posture over supine posture are discussed in [21]. Some authors also suggested compressing the breast to make it planar and more easily scanned [15], but this is what we want to avoid, since it may be painful and contrary to the contactless exam that we investigate in this paper.

The breast in prone position is non-symmetric. Nevertheless, few works have replicated the breast shape in their experimental tests. Indeed, most authors use a symmetric-shaped phantom to represent the breast [8], [22]- [24]. Symmetric-shaped breast allows using much simpler artifact removal and imaging algorithms that are not, however, applicable to anthropomorphic shapes. Yet, the symmetry assumption is not realistic and leads to poor results in real applications.

The use of symmetric antenna distribution illuminating the breast 1) simplifies the setup, 2) is easily adjustable to any breast size, and 3) helps decreasing costs by avoiding the use of complex positioning mechanisms. Nevertheless, it increases the difficulty of separating the tumor response from the measured signals, given that the antennas will be at different distances from the skin, as a consequence of the non-symmetric shape of the breast.

In summary, we experimentally demonstrate the correct operation of a MWI system using an anthropomorphic breast model in prone posture and a cylindrical antenna distribution without resorting to immersion medium. The breast includes fibroglandular tissues and, therefore, the dielectric constrast between healthy tissues and tumor is very much reduced. The image reconstruction algorithm relies on wave-migration [5], which was adopted due to its achievable accuracy, compatibility with the assumption of tissue dispersive properties and potential for real-time processing. To the authors' best knowledge, the present paper is the first experimental work successfully operating under all of these conditions.

This paper is organized as follows: in Sections II and III we address the problem formulation and signal processing, including the artifact removal and imaging algorithms. Section IV studies the impact of using an immersion liquid and concludes about the viability of imaging the body using a dry system. The experimental setup is described in Section V, including the antennas and phantom utilized in the measurements. The breast-shape estimation system and associated algorithms are presented in Section VI. The experimental results are discussed in Section VII and, finally, the main conclusions are drawn in Section VIII.

II. Problem Formulation

In microwave breast imaging, the tissues are illuminated by N_a probing antennas distributed around the breast, which transmit broadband signals and retrieve the echoes originated by the contrast between malignant and healthy tissues. In monostatic systems, the same antenna transmits and receives the signals; alternatively, one can use a single antenna as transmitter, while multiple antennas pick up the echoes at different coordinates – multistatic system. An example of the imaging scenario under study here is sketched in Fig. 1.

In this work we focus on MWI techniques for reflectivity map reconstruction based on monostatic observations. Such inverse problems may be described by the following matrix linear model [25]

$$\mathbf{g} = \mathbf{A}\mathbf{r} + \mathbf{w}, \tag{1}$$

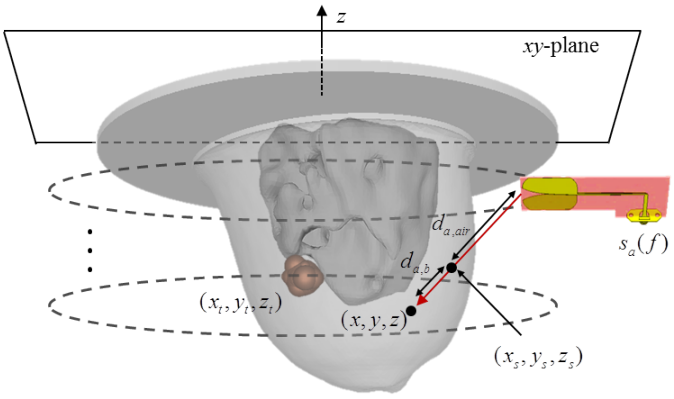

Fig. 1. Imaging domain representation with the antennas distributed around the breast in a cylindrical configuration.

where $\mathbf{r}$ is the sought reflectivity vector defined in suitable set of spatial coordinates,

$$\mathbf{r} = \begin{bmatrix} r(x_1, y_1, z_1) & r(x_1, y_1, z_2) & \dots & r(x_{N_x}, y_{N_y}, z_{N_z}) \end{bmatrix}^T \tag{2}$$

in which the operator $(.)^T$ denotes the transpose, and N_x, N_y, and N_z are the number of test points along each axis. In turn, $\mathbf{g}$ contains the measurements indexed by frequency and antenna position, $\mathbf{w}$ is an unknown perturbation vector, which we designate noise vector, that, in addition to additive noise, accounts for model uncertainties and degradations (such as the interference signal due to the air-skin interface), and matrix $\mathbf{A}$ is a linear operator accounting for the phase of the travelling wave. In more detail, we have

$$\mathbf{g} = \begin{bmatrix} \mathbf{s}_1^T & \dots & \mathbf{s}_a^T & \dots & \mathbf{s}_{N_a}^T \end{bmatrix}^T \tag{3}$$

where $\mathbf{s}_a = \begin{bmatrix} s_a(f_1) & \dots & s_a(f_{N_f}) \end{bmatrix}^T$ is the measured input reflection coefficient of the a-th antenna at coordinates (x_a, y_a, z_a) in the frequency band of interest $\Delta f = [f_1, f_{N_f}]$, where N_f designates the number of useful frequencies. The dimensions of $\mathbf{g}$ and $\mathbf{r}$ are $N_a N_f \times 1$ and $N_x N_y N_z \times 1$, respectively. For convenience, we may also denote the measured input reflection coefficient at a-th antenna by $s_a(f) = s(x_a, y_a, z_a, f)$.

Assuming the antenna to be a perfect radiator (i.e., with no internal reflections), only target point scatterers [26], and neglecting multiple reflections between the scatterers due to high losses of tissues, $\mathbf{A}$ is given by

$$\mathbf{A} = \begin{bmatrix} \mathbf{A}_1^T & \dots & \mathbf{A}_a^T & \dots & \mathbf{A}_{N_a}^T \end{bmatrix}^T \tag{4}$$

where $\mathbf{A}$ has dimensions $N_a N_f \times N_x N_y N_z$. In turn, each sub-matrix $\mathbf{A}_a$ is given by

$$\mathbf{A}_a = \begin{bmatrix} E(x_1, y_1, z_1, f_1)_a & \dots & E(x_{N_x}, y_{N_y}, z_{N_z}, f_1)_a \\ & \vdots & \\ E(x_1, y_1, z_1, f_{N_f})_a & \dots & E(x_{N_x}, y_{N_y}, z_{N_z}, f_{N_f})_a \end{bmatrix}, \tag{5}$$

in which the terms $E(x, y, z, f)_a$ account for the phase delay between the a-th antenna and the test point coordinate, (x, y, z), at frequency f, i.e.,

$$E(x, y, z, f)_a = \exp\{-2jk_0(f)[d_{a,air} + n_b(f) d_{a,b}]\}, \tag{6}$$

in which $k_0(f)$ is the free-space wavenumber of the propagating wave at frequency f, $n_b(f)$ is the dispersive refraction index of breast tissues, and $d_{a,air}$ and $d_{a,b}$ are the distances travelled by the radiated wave from the a-th antenna to the test point, (x, y, z), through air and tissues, respectively:

$$\begin{cases} d_{a,air} = \sqrt{(x_s - x_a)^2 + (y_s - y_a)^2 + (z_s - z_a)^2} \\ \\ d_{a,b} = \sqrt{(x_s - x)^2 + (y_s - y)^2 + (z_s - z)^2} \end{cases} \tag{7}$$

The coordinates (x_s, y_s, z_s) define the air-breast interface entry point (see Fig. 1). The dimensions of sub-matrix $\mathbf{A}_a$ are $N_f \times N_x N_y N_z$.

Note that in this formulation we considered the breast medium to be homogeneous, only captured by the term $n_b(f)$, since its internal structure is hardly known. Yet, this term can be adjusted according to some criteria, as to obtain the best imaging results [27]. Also, we assumed only scalar model. Both assumptions are common in medical MWI applications based on radar approaches. Lastly, we note that operator $\mathbf{A}$ does not account for the amplitude of the travelling wave, which is a multiplicative exponential term. The main reason for this is that the attenuation suffered by the waves in the breast tissue is difficult to estimate. As a result, if incorrectly estimated, even if just slightly, it may have a negative impact on the estimation of $\mathbf{r}$.

III. Signal Processing

This section discusses the signal processing algorithms used for the artifact removal and for the reflectivity map reconstruction of the breast tissues. We build up on the formulation described in the previous section, as it will be useful for the implementation of the algorithms.

A. Artifact removal algorithm

The following signal processing assumes that all signals retrieved in the presence of the breast have the free-space antenna input reflection coefficient subtracted. This correction step ensures that the unwanted antenna internal reflections are removed from the scattered signals, thus improving the measurable dynamic range [28].

To reduce the dominating short-distance skin backscattering that precludes the tumor detection, we extend the technique used in [8] based on Singular Value Decomposition (SVD). In that work, the analysis is restricted to uniform breast shapes, immersed in a coupling medium with the antenna at a constant distance from the skin. That greatly simplifies the application of the artifact removal algorithm. In the present work, we extend the method to more realistic setups by increasing its adaptability according to the retrieved signal reflection content.

Let us consider, for each antenna, the propagation scenario sketched in Fig. 2. There, d_s^{init} designates the shortest distance

between the antenna and the skin, d_s^{back}, the physical distance between opposite walls of the breast, and d_t is the distance from the skin to the tumor. The reflection coefficients of the front skin interface, opposite skin interface, and tumor are denoted by Γ_s^{init}, Γ_s^{back}, and Γ_t, respectively. The transmission coefficient of the skin (considered equal for inward and outward waves, apart from 180º phase shift) is denoted by T_s. Note that d_s^{init} is a particular case of $d_{a,air}$. For now, we consider an homogeneous breast. The method will be generalized to heterogeneous cases ahead.

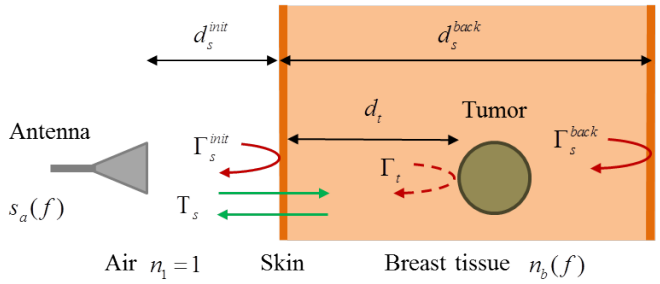

Fig. 2. Simplified propagation scenario for one antenna, used in the artifact removal formulation.

Building up on the assumptions discussed in Section II, the measured signals in the scenario sketched in Fig. 2, and in the absence of noise, are well approximated by a sum of complex exponentials [26] described as

$$\begin{aligned} s_a(f) = {} & c^{init}\exp\left(-2jk_0 d_s^{init}\right) \\ & + c_t\exp\left[-2jk_0\left(d_s^{init}+n_b d_t\right)\right] \\ & + c^{back}\exp\left[-2jk_0\left(d_s^{init}+n_b d_s^{back}\right)\right] \end{aligned} \tag{8}$$

where $c^{init} = \chi^{init}\Gamma_s^{init}$, $c_t = \chi_t T_s^2 \Gamma_t$, and $c^{back} = \chi^{back} T_s^2 \Gamma_s^{back}$ are coefficients related to the reflection, transmission, and dissipation losses, respectively, all dependent on body material properties, as well as the radial spreading of the propagating spherical wave, χ. Each term in (8) corresponds to a single scatterer. Moreover, since $\left|c^{init}\right| \gg |c_t|$ and $\left|c^{init}\right| \gg \left|c^{back}\right|$, then the first term on the right hand side of (8) dominates $s_a(f)$, which hinders the estimation of the second term, corresponding to the tumors. It is important to take into account the reflection on the back skin interface, so that the algorithm is robust to fatty, less dense breasts. We will show that this coefficient does not have any relevant impact when the breast is denser.

The terms on the right hand side of (8) have the structure $\gamma_i(f) = c_i(f)\, e^{-j\beta_i f}$ for $i = 1,2,3$ with $c_1(f) = c^{init}(f)$, $c_2(f) = c_t(f)$ and $c_3(f) = c^{back}(f)$, $\beta_1 = (4\pi/v)\, d_s^{init}$, $\beta_2 = (4\pi/v)\left(d_s^{init} + n_b d_t\right)$, and $\beta_3 = (4\pi/v)\left(d_s^{init} + n_b d_s^{back}\right)$, where v is the speed of light in vacuum. If f is assumed to take values in the interval $\Delta f = \left[f_1, f_{N_f}\right]$ that $c_i(f)$ is smooth in Δf, that β_i for $i = 1,2,3$ are different, and that $\beta_1 \Delta f \gg 2\pi$, then the terms $\gamma_i(f)$ for i = 1, 2, 3 are orthogonal and may be filtered out in the frequency domain. However, the last condition is not satisfied at least for signal $\gamma_1(f)$; as an example, take $\Delta f = 3$ GHz and $d_s^{init} = 10$ mm thus yielding $\beta_1 \Delta f = 0.4$ rad. Therefore, the signal $\gamma_1(f)$ cannot be filtered out in the frequency domain.

We attack the filtering problem just described with the SVD [31], which factorizes any matrix $\mathbf{M}$ of size $m \times l$ as

$$\mathbf{M} = \mathbf{U}\boldsymbol{\Sigma}\mathbf{V}^H, \tag{9}$$

where $(.)^H$ denotes the Hermitian operator $\mathbf{U} = [\mathbf{u}_1|\mathbf{u}_2|\ldots|\mathbf{u}_m]$ of size $m \times m$ and $\mathbf{V} = [\mathbf{v}_1|\mathbf{v}_2|\ldots|\mathbf{v}_l]$, of size $l \times l$ that hold the vectors $\mathbf{u}_i$, for $i = 1,\ldots,m$ and $\mathbf{v}_i$, for $i = 1,\ldots,l$, are the left- and right-singular vectors respectively, forming two orthonormal basis of the space spanned by the columns and rows of $\mathbf{M}$, respectively. The matrix $\boldsymbol{\Sigma}$ is diagonal and contains the singular values, $\sigma \geq 0$, in non-increasing magnitude. Among the various applications of SVD, the best q-rank approximation of matrix $\mathbf{M}$, which minimizes the Frobenius norm, $\|\mathbf{M}_q - \mathbf{M}\|_F$, is calculated as

$$\mathbf{M}_q = \sum_{i=0}^{q} \sigma_i \mathbf{u}_i \mathbf{v}_i^H, \tag{10}$$

where $(\sigma_i, \mathbf{u}_i, \mathbf{v}_i)$, for $i = 0,\ldots,q$, are the first q singular values, left singular vectors, and right singular vectors, ordered by non-increasing value of σ_i. Below, we exploit the low-rank approximation property of the SVD in the direction (or directions) of maximum power corresponding to the skin signal.

Contrarily to [8], we drop the assumption of uniform breast shapes. Yet, we still assume locally smooth shapes, which imply that the skin backscattering is locally identical; i.e., within a region of $2 \times N_n$ neighbor antennas relative to the a-th central position, the antennas "see" similar skin responses [30]. To take advantage of this assumption, we arrange the $\mathbf{S}_a$ matrix containing the $(2 \times N_n + 1)$ input reflection coefficients versus frequency, centered at the a-th antenna, as

$$\mathbf{S}_a = \begin{bmatrix} \mathbf{s}_{a-N_n} & \ldots & \mathbf{s}_a & \ldots & \mathbf{s}_{a+N_n} \end{bmatrix}. \tag{11}$$

Based on expression (8), each of the columns of $\mathbf{S}_a$, i.e., $\mathbf{s}_p$, for $p = a - N_n, \ldots, a + N_n$, may be written as the sum of three terms:

$$\mathbf{s}_p = \boldsymbol{\gamma}_{p,1} + \boldsymbol{\gamma}_{p,2} + \boldsymbol{\gamma}_{p,3}, \tag{12}$$

where $\boldsymbol{\gamma}_{p,1}$, $\boldsymbol{\gamma}_{p,2}$ and $\boldsymbol{\gamma}_{p,3}$ correspond to the signals originated by the skin (closest to the antenna), tumor and skin (farthest to the antenna), respectively. Given the above referred similarity, vector $\boldsymbol{\gamma}_{p,1}$ is almost constant for $p = a - N_n, \cdots, a + N_n$ since in this interval their elements present only slight variations of the distance between the antenna and the skin. Therefore the elements of $\boldsymbol{\gamma}_{p,1}$ have common β_i across the region around $2N_n$ neighboring antennas. The same happens for $\boldsymbol{\gamma}_{p,3}$. However, since β_i are different for $\boldsymbol{\gamma}_{p,1}$, $\boldsymbol{\gamma}_{p,2}$ and $\boldsymbol{\gamma}_{p,3}$, this makes them orthogonal. Moreover, since $\left|c^{init}\right| \gg |c_t|$, we assume that $\boldsymbol{\gamma}_{p,1}$ has norm much greater than the norm of $\boldsymbol{\gamma}_{p,2}$. At some antenna positions the reflection on the back skin wall is also greater than the tumor response, i.e. $\left|c^{back}\right| > |c_t|$.

Fig. 3 schematizes the relative location of vectors $\mathbf{s}_p$. There, $\widehat{\mathbf{s}}_{p,1}$ designates the projection of $\mathbf{s}_p$ onto the subspace orthogonal to span$(\mathbf{u}_1, \ldots, \mathbf{u}_q)$. Vector $\widehat{\mathbf{s}}_{p,2}$, which is the projection of

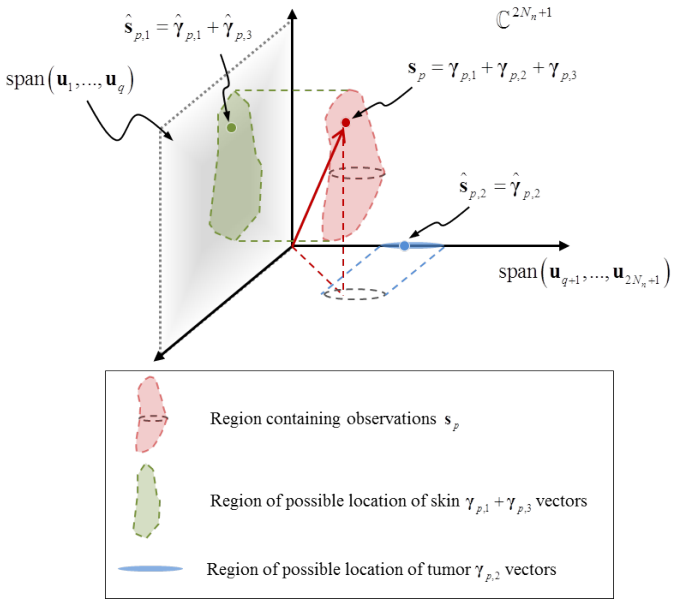

Fig. 3. Relative location of vectors $\mathbf{s_p}$, $\boldsymbol{\gamma}_{p,1}$, $\boldsymbol{\gamma}_{p,3}$ (skin), and $\boldsymbol{\gamma}_{p,2}$ (tumor) for different antenna locations in a given neighborhood. Vector $\widehat{\boldsymbol{\gamma}}_{p,2}$ is the projection of $\mathbf{s_p}$ onto the subspace orthogonal to span$(\mathbf{u}_{q+1}, \ldots, \mathbf{u}_{2N_n+1})$ and is close to $\boldsymbol{\gamma}_{p,2}$.

$\mathbf{s}_p$ onto the subspace orthogonal to span$(\mathbf{u}_{q+1}, \ldots, \mathbf{u}_{2N_n+1})$, is close to $\gamma_{p,2}$ and has the bulk of the skin response removed.

In order to explore the properties of $\mathbf{s}_p$, matrix $\mathbf{S}_a$ is factorized using the SVD. According to the above rationale, and since $\left|c^{init}\right| \gg |c_t|$ and $\left|c^{init}\right| \gg \left|c^{back}\right|$, then the initial reflection on the skin is well-approximated by the first singular value, which has the greatest magnitude. We then project $\mathbf{S}_a$ onto the orthogonal subspace spanned by the first q singular vectors $\mathbf{U}_q = [\mathbf{u}_1 \ \ldots \ \mathbf{u}_q]$, where q is to be determined according to some criteria. This way, we get the calibrated matrix (i.e. without the skin artifact), $\mathbf{S}_a^{cal}$, by subtracting the contribution from the unwanted q scatterers:

$$\mathbf{S}_a^{cal} = \mathbf{S}_a - \sum_{i=0}^{q} \sigma_i \mathbf{u}_i \mathbf{v}_i^H \tag{13}$$

Therefore, the calibrated matrix contains the frequency response of the inner tissues only, for the a-th antenna position. From $\mathbf{S}_a^{cal}$ we extract the frequency response corresponding to the central antenna a, $\mathbf{s}_a^{cal}$. Note that if q = 0 we remain with the original signal, which contains the initial skin reflection. In the opposite scenario, if we remove all the q singular values $\min(2 \times N_n + 1, N_f)$, where the number of frequencies is generally much greater than the number of antenna positions, the filtered signal becomes zero.

In [8] not only the skin reflection was assumed to be the same across all the antenna positions, but also the value of q was taken constant. Nevertheless, in a realistic non-uniform breast scenario, q cannot be considered equal for all antennas. In fact, q in (13) needs to be adapted for each antenna position, since the skin reflection varies significantly along the spatial scan. We propose an iterative method to automatically set q for each antenna position. We start by considering q = 0. The signals are then converted to the spatial domain by means of the Inverse Discrete Fourier Transform (IDFT), from which we obtain $s_{a,0}(d)$, where d is the roundtrip distance. This allows estimating the initial skin reflection distance, d_s^{init}. Then, we increment q, and apply the SVD followed by the IDFT to calculate $s_{a,1}(d)$. The process is repeated, and q is incremented, until the maximum of $s_{a,q}(d)$ falls out of the breast walls. These are defined by the electric length intervals $\left[d_s^{init} - \Delta d, d_s^{init} + \Delta d\right]$ and $\left[d_s^{init} + n_b^{avg} d_s^{back} - \Delta d, d_s^{init} + n_b^{avg} d_s^{back} + \Delta d\right]$, where n_b^{avg} represents the average frequency dependent refractive index of the breast tissues and Δd is the theoretical range resolution of the imaging system in the breast tissues [32]

$$\Delta d = \frac{v}{4 n_b^{avg} \Delta f}. \tag{14}$$

This procedure is repeated for all N_a antenna positions. In the end, we merge the $\mathbf{s}_a^{cal}$ in the according order into a single matrix,

$$\mathbf{S}^{cal} = \left[\mathbf{s}_1^{cal} \ \ldots \ \mathbf{s}_a^{cal} \ \ldots \ \mathbf{s}_{N_a}^{cal}\right]. \tag{15}$$

in which $\mathbf{s}_a^{cal}$ is defined along frequency, $\mathbf{s}_a^{cal} = \left[s_a^{cal}(f_1) \ \ldots \ s_a^{cal}\left(f_{N_f}\right)\right]^T$. This method falls into the data adaptive class of artifact removal algorithms, since the orthogonal subspace is learned from the measured input reflection coefficients.

We highlight that the proposed procedure to define q can be easily automated. Furthermore, it is computationally fast, making it compatible with real-time systems, and it does not introduce any distortion in the tumor position. Lastly, it is capable of detecting tumors at distances from the skin below the theoretic image resolution (equation (14)), as will be shown ahead. The latter is an important feature of this artifact removal, since many algorithms struggle under these conditions, in particular those based on time/spatial gating techniques.

From this point onwards, we modify the observation model in (1) to accommodate the impact of the artifact removal, as follows

$$\mathbf{g}^{cal} = \mathbf{A}\mathbf{r} + \mathbf{w}^{cal}, \tag{16}$$

where $\mathbf{w}^{cal}$ corresponds to the noise after the air-skin interference has been removed, and $\mathbf{g}^{cal}$ is the corresponding vector of observations.

As an example of the proposed iterative artifact removal algorithm, let us consider the two-dimensional numerical setup depicted in Fig. 4, which was simulated using Computer Simulation Technology (CST) Microwave Transient Solver [33]. It consists of a simplified cylindrical breast phantom with elliptical cross-section illuminated by a broadband bowtie antenna [34]. The breast model includes a 0.7 mm thick skin layer and homogeneous fatty tissues with complex permittivity of $\epsilon_s = 36 - j3.4$ and $\epsilon_{fat} = 7.34 - j0.24$ at 3.5 GHz, respectively. The tumor, also cylindrical, is located at coordinates (x, y) = (15, 10) mm and has a complex permittivity of $\epsilon_{tmr} = 40.7 - j4$ at 3.5 GHz. Later on, we perform an additional simulation with the same breast shape and tumor, but considering heterogeneous breast filling with xy cross-section depicted in the inset in Fig. 4. These tissues intend to represent the higher-density fibroglandular tissues

of the breast, which we assume to have a permittivity of $\epsilon_{fg} = 30.5 - j3$ [14].

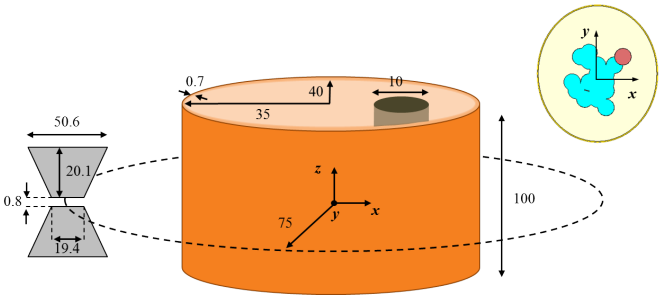

Fig. 4. Two-dimensional numerical setup used to exemplify the application of the proposed artifact removal algorithm (dimensions in millimeters). The top right close-up represents the xy-cross-section of the heterogeneous breast used in the numerical tests.

The used bowtie antenna operates in the 2-5 GHz range ($|S_{11}| \leq -10$ dB). A total of N_a = 24 antenna positions are considered around the breast, distributed over a circle of radius 75 mm centered at $(0, 0, 0)$. As a consequence of the breast elliptical shape, the antenna-to-breast distance, d_s^{init}, varies between 35 mm and 40 mm. We applied the proposed artifact removal to the above homogeneous model considering N_n = 2, Δf = 3 GHz and N_f = 34 frequencies. The corresponding theoretical resolution in the breast tissue, given by (14), is 9.2 mm.

An example of the spatial signals, $s_{a,q}(d)$, from which the value of q was determined, is presented in Fig. 5. At the illustrated position, d_s^{init} = 39 mm, d_s^{back} = 72 mm and d_t = 36 mm approximately. The abscissa in this figure represents the electrical distance. The vertical dashed lines identify the front and back breast walls, whereas the red circle identifies the electrical tumor distance. Note that the distance of the skin reflections is assumed to be known – this subject is handled in section VI.

First, we note that q = 1 is enough to successfully remove the initial skin reflection. However, the tumor is still masked by the reflection on the opposite wall. By filtering another singular vector, the second skin reflection is mitigated and the tumor is observable at the correct distance (red circle). A maximum is still observable near the back wall, but the same does not happen for the other antenna positions. Therefore, the imaging reconstruction algorithm, presented in the next sub-section, inherently filters it out.

B. Image reconstruction algorithm

The imaging problem that we face aims at solving the inverse problem under the linear observation model (16). Its final objective is to estimate the reflectivity of the breast tissues, $\mathbf{r}$. In this sub-section, we formulate an imaging algorithm based on wave-migration approach to get a useful estimation of $\mathbf{r}$, $\widehat{\mathbf{r}}$, thus allowing detecting the tumor.

The present imaging inverse problem is quite challenging due to its ill-posedness. The reasons that account to this are:

1) The presence of noise and model uncertainties captured by the term $\mathbf{w}^{cal}$. We have identified at least three sources of uncertainties that contribute to the term $\mathbf{w}^{cal}$. Firstly, the microwave energy refracts at the breast boundary. However, we are considering only direct ray propagation for the sake of simplicity and computational effort. We note that this is common practice in MWI based on radar algorithms [26]. Secondly, we assume static antenna phase center. Nevertheless, the phase center moves with frequency and depends on angle of arrival, leading to errors in the calculation of distances [28]. Lastly, the variability of the permittivity of the internal tissues that is not possible to predict which also accounts to the errors.
2) Matrix $\mathbf{A}$ is fat, corresponding to an under-determined system of equations.
3) The number of singular values of $\mathbf{A}$ with significant magnitude, N_σ, is considerably smaller than the number of rows in $\mathbf{A}$, N_{rows}. As an example, Fig. 6 shows the singular values of $\mathbf{A}$ calculated based on the two-dimensional scenario depicted in Fig. 4. In this case, we have considered $N_x = 61$, $N_y = 61$ and $N_z = 1$ (two-dimensional example), while keeping N_a and N_f unchanged. The number of rows of $\mathbf{A}$ in this example is $N_{rows} = N_a N_f = 24 \times 34 = 816$, but N_σ is around 100, thus proving this is a challenging inverse problem.

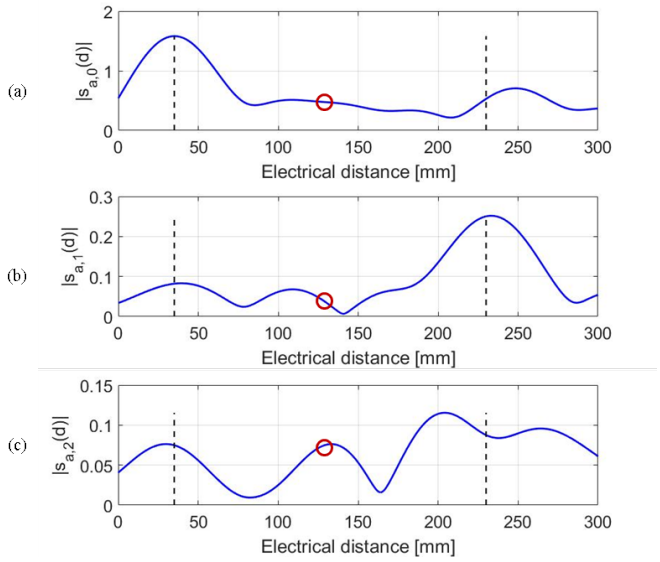

Fig. 5. Example of $s_{a,q}(d)$ for different q values: (a) q = 0; (b) q = 1; (c) q = 2. These results correspond to a single antenna position. The vertical dashed lines identify the electrical distance of the front and back breast walls, whereas the red circle identifies the actual tumor distance.

Such an ill-posed inverse problem calls for regularization. However, the quality of the inference obtained by solving an inverse problem relies strongly on the quality of the direct model. This is not the case in the problem in hands, owing to the uncertainties captured by the term $\mathbf{w}^{cal}$. As a result, we solve this problem through a matched-filter approach. Although matched-filter does not provide the best resolution, it is robust to model errors and yields the best signal-to-noise ratio [35]. This way, we are able to retrieve reliable information about the presence of tumors inside the breast.

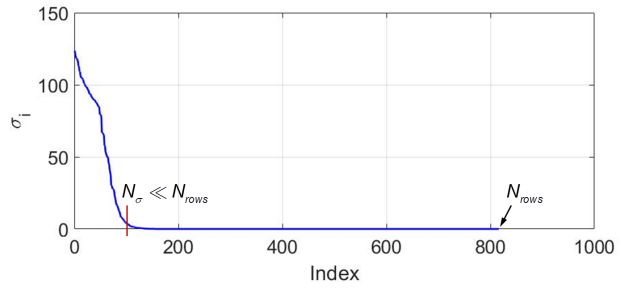

Fig. 6. Singular values of $\mathbf{A}$, σ_i, calculated from the numerical example shown in Fig. 4.

As such, the reflectivity map is estimated as

$$\widehat{\mathbf{r}} = \mathbf{A}^H \mathbf{g}^{cal} \tag{17}$$

Hence, each element i of $\widehat{\mathbf{r}}$ can be calculated as

$$\begin{aligned} \widehat{r}_i &= \mathbf{a}_i^H \mathbf{g}^{cal} \\ &= \sum_{a}^{N_a} \sum_{f}^{N_f} g_{a,f}^{cal} \exp\left\{2jk_0(f)\left[d_{a,b}n_b(f) + d_{a,air}\right]\right\} \end{aligned} \tag{18}$$

in which $d_{a,b}$ and $d_{a,air}$ are defined according to eq. (7), and $g_{a,f}^{cal}$ is the calibrated input reflection coefficient at frequency f measured at antenna a after the skin reflection has been removed. Since we do not have prior knowledge of the internal structure of the breast, the reconstruction algorithm assumes propagation in homogeneous medium inside the breast, accounted by term n_b that may be dispersive.

Lastly, given that $\widehat{\mathbf{r}}$ is defined over a known volume, the intensity of each pixel forming the image, $I(x, y, z)$, is proportional to the power of the backscattered signals at each coordinate (x, y, z), i.e.,

$$I(x, y, z) \propto \left|\widehat{\mathbf{r}}\right|^2. \tag{19}$$

C. Performance metrics

We use quantitative figures of merit to assess the quality of the image reconstruction algorithm and to perform comparisons between available methods.

1) Imaging quality metrics: The tumor-to-clutter ratio (TCR) and tumor-to-mean ratio (TMR) assess the imaging detection quality [36]. TCR compares the maximum intensity corresponding to the tumor response (T) and the larger unwanted artifact intensity (clutter – C) occurring anywhere in the whole 3D reconstructed image:

$$\text{TCR}\,[\text{dB}] = 10\log_{10}\left[\frac{\max(T)}{\max(C)}\right] \tag{20}$$

Additionally, the TMR evaluates the ratio between the intensity of the tumor response and the mean intensity of the background medium response:

$$\text{TMR}\,[\text{dB}] = 10\log_{10}\left[\frac{\max(T)}{\text{mean}(C)}\right] \tag{21}$$

2) Tumor detection metric: Lastly, we compute two metrics to assess the ability of the overall signal processing to detect the tumor in the correct position. To this end, we use the positioning error (PE), which quantifies the deviation of the detected tumor, $P_{detection}$, position with respect to the actual position, P_{tumor}, known from the measurement setup:

$$\text{PE} = \|P_{tumor} - P_{detected}\| \tag{22}$$

Additionally, we calculate the normalized PE, NPE, relative to the theoretical resolution of the imaging system, Δd (expression (14)):

$$\text{NPE} = \frac{\text{PE}}{\Delta d} \tag{23}$$

We applied the described imaging algorithm to the numerical results obtained from the setup shown in Fig. 4, after using the proposed artifact removal algorithm. The reconstructed images for the homogeneous and heterogeneous breasts are represented in Fig. 7 (a) and (b), respectively. The small white circle marks the actual position of the tumor. The results show very good tumor detection in both scenarios. For the homogeneous breast we obtained TCR = 3.44 dB, TMR = 10.2 dB, PE = 3.6 mm, and NPE = 0.39; whereas for the heterogeneous breast, TCR = 1.54 dB, TMR = 9.7 dB, PE = 7.3 mm, and NPE = 0.8. In both cases, the error in the tumor position is better than the theoretical resolution of the system. Moreover, the imaging results slightly deteriorate with the presence of the fibroglandular tissues, which decrease the contrast between tumor and background medium, and also increase the signals backscattered inside the breast.

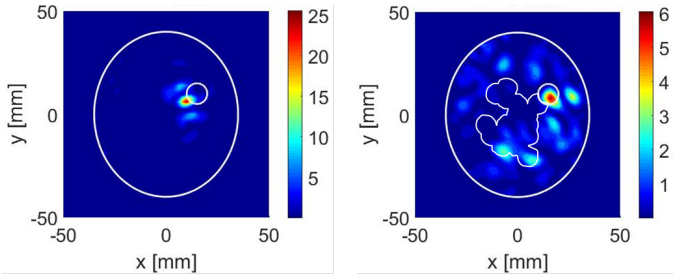

(a) (b)

Fig. 7. Two-dimensional image obtained from the numerical results: (a) homogeneous breast; (b) ACR-3 heterogeneously dense breast. The outer white contour identifies the breast shape and the smaller white circle identifies the actual tumor position.

IV. Quantification of Immersion Liquid Impact on Skin Reflection

The use of a dense coupling medium between antennas and breast in Medical MWI systems is common practice among research works, as explained in the Introduction [7]- [9]. In order to conclude about the real need of a coupling medium, we analyze the skin reflection using a cascaded transmission line model (TLM), see Fig. 8. The TLM provides useful information about the energy reflected by the skin and the energy coupled to the breast. Each transmission line section represents a propagation medium: background, skin, fat and

fibroglandular. The cascade of tissues should approximate reasonably the internal structure of the breast, given that fat is immediately below the skin, whereas fibroglandular tissues are internal. A similar study was performed in [37], but considering homogeneous breast with high density. We emphasize that the results presented in this section were validated by full wave simulations using CST (not shown here for conciseness).

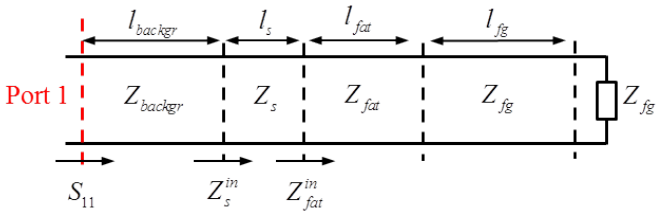

Fig. 8. Schematic of the transmission line model used to study the impact of the immersion liquid in mitigating the energy reflected from the skin and energy coupled to the body.

The impedance of each medium is defined as $Z_{medium}(f) = \sqrt{\mu_0/[\epsilon_0\epsilon_{medium}(f)]}$ where μ_0 and ϵ_0 are the permeability and permittivity of vacuum, respectively, and $\epsilon_{medium}(f) = \epsilon'_{medium}(f) - j\epsilon''_{medium}(f)$ is the complex relative permittivity of each medium. For simplicity, the equations will not show onwards the dependence on frequency. The propagation constant is written as $\kappa_{medium} = j\omega\sqrt{\mu_0\epsilon_0\epsilon_{medium}}$ given that $\mu_r = 1$ for all involved materials. Parameter ω designates the angular frequency, $\omega = 2\pi f$. We considered constant permittivity of tissues across frequency, with values of $\epsilon_s = 37 - j10.36$, $\epsilon_{fat} = 8 - j0.8$, $\epsilon_{fg} = 48 - j9.6$, for the skin, fat and fibroglandular tissues, respectively. These dielectric properties correspond to the approximate properties of each tissue at 3.5 GHz, according to references [40] and [14], respectively. For the purpose of this study, the permittivity of the background medium, ϵ_{backgr}, is swept between 1 and 100 with loss tangent of $tan(\delta) = \frac{\epsilon''_{backgr}}{\epsilon'_{backgr}} = 0.01$.

According to transmission line theory, the magnitude of input reflection coefficient, $|S_{11}|$, of the TLM shown in Fig. 8 is given by

$$|S_{11}| = |\Gamma| = \left|\frac{Z_s^{in} - Z_{backgr}}{Z_s^{in} + Z_{backgr}}\right| \tag{24}$$

where input impedance at the background/skin interface is given by $Z_s^{in} = Z_s\frac{Z_{fat}^{in} + Z_s\tanh(\kappa_s l_s)}{Z_s + Z_{fat}^{in}\tanh(\kappa_s l_s)}$, and, lastly, the input impedance at the fat/fibroglandular interface is given by $Z_{fat}^{in} = Z_{fat}\frac{Z_{fg} + Z_{fat}\tanh(\kappa_{fat} l_{fat})}{Z_{fat} + Z_{fg}\tanh(\kappa_{fat} l_{fat})}$. These parameters take into account the losses in each dielectric.

We assume that the distance between the excitation port and skin is l_{backgr} = 20 mm and breast path length is l_{fat} = 35 mm and l_{fg} = 40 mm. Regarding the skin thickness, l_s, reference [42] reports that the minimum thickness for a healthy breast is around 0.7 mm. On the contrary, a diseased breast can have 2.5 mm skin thickness. For the purpose of the present study we present results for both thicknesses. As for the frequency range, we analyzed the bandwidth from 1 GHz up to 6 GHz, which is the most commonly used bandwidth for breast imaging. Fig. 9 presents the numerical results based on TLM of the backscattered power at the background medium/skin interface, $|S_{11}|^2$.

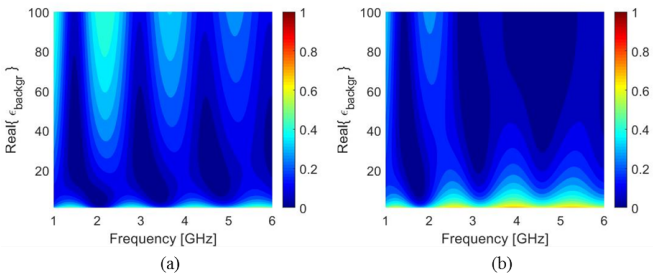

Fig. 9. Skin backscattered power, $|S_{11}|^2$, computed analytically based on the TLM illustrated in Fig. 8: (a) l_s = 0.7 mm; (b) l_s = 2.5 mm.

Although the results in Fig. 9 provide useful information about the impact of the coupling medium for a wide range of values of ϵ_{backgr}, for the purpose of this paper let us concentrate our analysis on three cases: $\epsilon'_{backgr} = 1$, $\epsilon'_{backgr} = 3$, and $\epsilon'_{backgr} = 30$. The first represents the dry setup we seek, the second represents the immersion in canola oil, which is common practice in medical MWI [38], [39], and the last represents the case which was identified by the authors of reference [37] as the best case scenario to minimize the reflection on the skin. These results are summarized in Table I.

TABLE I
SUMMARY OF IMMERSION LIQUID STUDY VERSUS FREQUENCY, $|S_{11}|^2$, FOR $\epsilon'_{backgr} = 1$, $\epsilon'_{backgr} = 3$, AND $\epsilon'_{backgr} = 30$.

$l_s = 0.7$ mm						
	1 GHz	2 GHz	3 GHz	4 GHz	5 GHz	6 GHz
$\epsilon'_{backgr} = 1$	0.31	0.13	0.44	0.45	0.34	0.47
$\epsilon'_{backgr} = 3$	0.16	0.01	0.24	0.26	0.15	0.27
$\epsilon'_{backgr} = 30$	0.24	0.18	0	0.11	0.07	0.02
$l_s = 2.5$ mm						
	1 GHz	2 GHz	3 GHz	4 GHz	5 GHz	6 GHz
$\epsilon'_{backgr} = 1$	0.52	0.43	0.56	0.70	0.66	0.58
$\epsilon'_{backgr} = 3$	0.34	0.24	0.37	0.54	0.49	0.39
$\epsilon'_{backgr} = 30$	0.2	0.11	0.02	0.13	0.09	0.05

We quantified the skin reflection ratio (SRR) as the ratio between the average of the reflected power over the entire frequency band $[1, 6]$ GHz for given values of l_s, and ϵ'_{backgr}, and the average for $\epsilon'_{backgr} = 1$:

$$SRR_{dB} = 10\log_{10}\left\{\frac{avg\left[\left|S_{11}\left(l_s, \epsilon'_{backgr}\right)\right|^2\right]}{avg\left[\left|S_{11}\left(l_s, \epsilon'_{backgr} = 1\right)\right|^2\right]}\right\} \tag{25}$$

This indicator gives a measure of the skin reflection reduction by the coupling media compared to the dry case. The maximum SRR for a breast immersed in oil is about -2.75 dB obtained for $l_s = 0.7$. In turn, for $\epsilon'_{backgr} = 30$ the skin suppression improves at most -7.92 dB obtained for $l_s = 2.5$.

These values should be analyzed in light of the noise floor of the measurement setup. To this end, we have measured the noise floor of our dry experimental setup (to be described in section V), and concluded that an increase of skin reflection up to 8 dB does not preclude the use of dry imaging setups, since the tumor response after applying our artifact removal should be well above the noise floor. As a result, the use of immersion liquid only partially tackles the skin artifact challenge, therefore making its use not imperative. Based on this conclusion, we have developed an imaging system without immersion liquid, which we will address in the remaining of this paper.

However, for practical reasons related to the 3D-printing fabrication method, the skin of our experimental breast phantom does not present the actual skin electrical properties. Instead, its refractive index is $n_s = \sqrt{2.75}$ [43] corresponding to PLA plastic. Of course, this raises the doubt of representativeness of such model in the present context. In order to clear that, we have repeated the S_{11} study for the "air-PLA-fat-fibroglandular" scenario, considering the skin thickness parameter fixed at l_s = 1.2 mm. The results are plotted in Fig. 10. For better comparison, we superimpose in the same figure the $|S_{11}|^2$ curves for $l_s = 0.7$ mm and $l_s = 2.5$ mm, already plotted in Fig. 9, calculated for $\epsilon'_{backgr} = 1$ (dry setup).

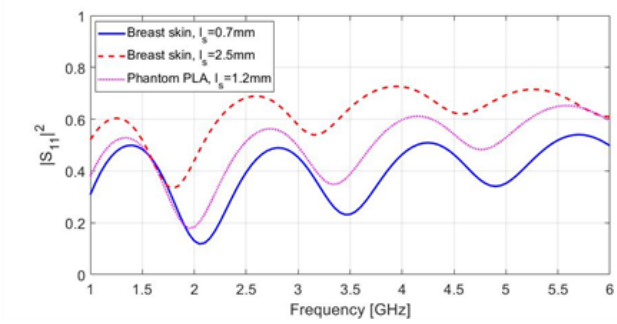

Fig. 10. Backscattered power, $|S_{11}|^2$, computed analytically based on the TLM illustrated in Fig. 8 for l_s = 0.7 mm and l_s = 2.5 mm, and also considering the experimental 3D-printed breast phantom, where the skin is represented by PLA (l_s = 1.2 mm, $n_s = \sqrt{2.75}$). For all curves, $\epsilon'_{backgr} = 1$.

In order to assess the representativeness of the plastic breast relative to the real case, we calculated the SRR of curves represented in Fig. 10, where the numerator is the $\left|S_{11}\left(l_s, \epsilon'_{backgr} = 1\right)\right|^2$ for $l_s = 0.7$ mm or $l_s = 2.5$ mm, and the denominator is the $\left|S_{11}\left(l_s = 1.2 \text{ mm}, \epsilon'_{backgr} = 1\right)\right|^2$ considering $n_s = \sqrt{2.75}$. For l_s = 0.7 mm the SRR is about 0.9 dB, which means that the PLA breast reflects more energy than the real breast. As for thicker skin value, l_s = 2.5 mm, the SRR is approximately -1.04 dB. These values show that the PLA breast is a reasonable approximation to a realistic breast and, therefore, the algorithms and measurements described in this paper should be representative of the real examination scenario.

V. Experimental Setup

In this section we describe our experimental dry setup. Moreover, we demonstrate the feasibility of a functional miniaturized antenna, despite not benefiting from a dense immersion medium.

A. Breast phantoms

For the experimental tests we use a MRI-derived breast phantom taken from the University Wisconsin-Madison repository (ID: 062204) [44], corresponding to American College of Radiology (ACR) 3 classification - heterogeneously dense breast. We 3D printed it using polylactic acid (PLA, ϵ_r = 2.75 [43] on a Ultimaker 2+ Extended [45]). The model includes the breast shell, with 1.2 mm wall thickness, the fibroglandular container - Fig. 11 (a) and the tumor - an ellipsoidal container with the internal dimensions depicted in Fig. 11 (b). The 3D printer settings used for the tumor container were the same as for the remaining parts. We highlight that the breast repository of the University of Wisconsin-Madison is accepted in the literature as fair representation of actual breasts for the different ACR classification in terms of density.

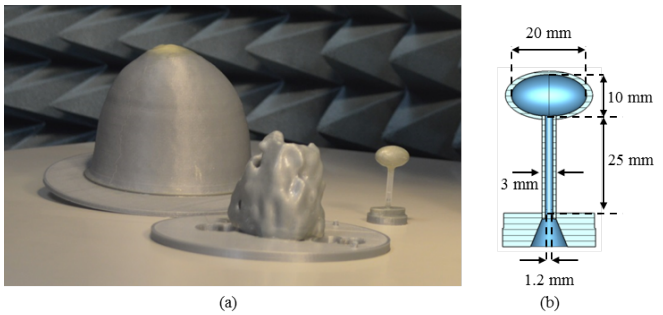

Fig. 11. 3D-printed phantom used in the experimental setup: (a) breast phantom; (b) internal dimensions of the tumor container.

The containers were filled with different mixtures of TX-100, distilled water and sodium chloride (NaCl) that approximate the dielectric properties of breast and tumor tissues. The recipes were taken from [46]. We measured the complex permittivity of the mixtures using the cavity method described in [47]. Fig. 12 presents the results of the dielectric constant and equivalent conductivity. The latter is calculated as $\sigma_e = \omega\epsilon_0\epsilon''$. The agreement between phantom liquids and the real tissues is reasonably good.

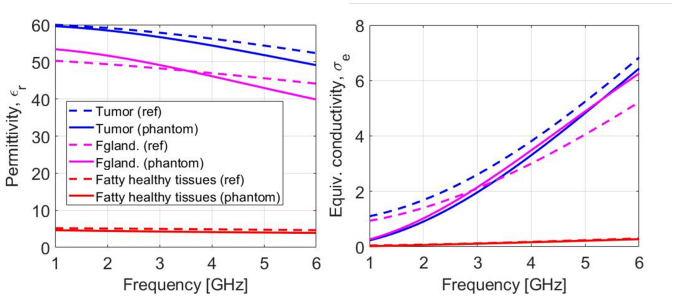

Fig. 12. Permittivity and equivalent conductivity of healthy fatty tissues, fibroglandular tissues and tumor taken from [40] and [14] (dashed lines), respectively, and of liquid phantoms used in measurements (solid lines).

B. Antenna design and antenna distribution

We opted for a Balanced Antipodal Vivaldi Antenna (BAVA), printed on a RT/duroid 6010 substrate (ϵ_r = 10.2, tan(δ) = 2.3 $\times 10^{-3}$) of thickness 25 mils (0.635 mm). The antenna topology falls within the class of travelling-wave, end-fire antennas that cover a wide frequency spectrum [48]. Furthermore, its small cross-section minimizes the undesired interactions between the breast and antenna.

The geometry of our BAVA is detailed in Fig. 13. It consists of two antipodal exponential "fins" capped by truncated ellipses to achieve a compact antenna design [49]. Two exponential curves of the form

$$\begin{cases} E_t(v) = \pm A_t \exp(P_t v) + C_t \\ E_a(u) = \pm A_a \exp(P_a u) + C_a \end{cases} \tag{26}$$

describe the "fins" and the feeding microstrip line [39]. Thirteen other parameters, marked in Fig. 13, define the remainder geometry. The fine-tuning of all parameters was achieved through full-wave simulation using CST Microwave Transient solver [33]. One of the optimization goals was to achieve an input reflection coefficient below -15 dB ($|S_{11}| \leq$ -15 dB) between 2.5 GHz and 5 GHz. This frequency interval offers the best trade-off between penetration depth, image resolution, and antenna size. The second goal (results not shown for the sake of conciseness), was to ensure that the radiation maximum is directed towards the u-axis.

The optimized values of coefficients A_a, C_a, P_a, A_t, C_t, and P_t are presented in Table II, along with the remaining geometry parameters.

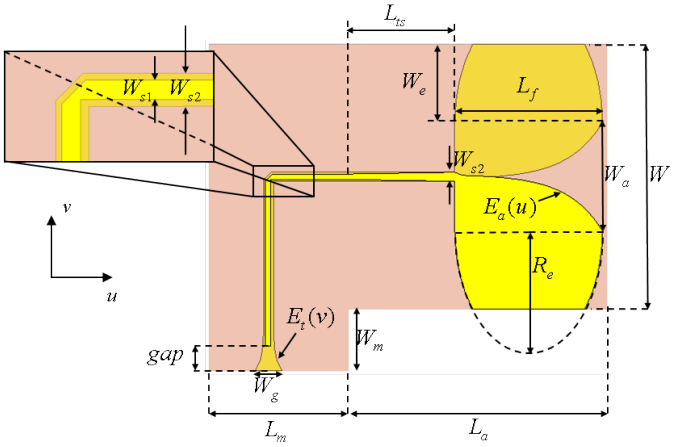

Fig. 13. Geometry of the designed BAVA for MWI.

TABLE II
BAVA GEOMETRY PARAMETERS DIMENSIONS IN MILLIMETERS.

A_a	C_a	P_a	W	W_a	W_m	W_g	W_{s1}	W_{s2}	W_e
0.141	0.41	0.17	44.46	28.6	10.3	8.99	0.93	1.53	13.1
A_t	C_t	P_t	L_a	L_{ts}	L_f	L_m	R_e	gap	
0.108	0.77	-0.131	43.34	17.74	24.8	23.56	40.3	3.9	

The 90º mitre bend in the microstrip line ensures that the feeding connector has minimal influence on the antenna performance, which also contributes to improve the S_{11}. The bandwidth is reasonably achieved, as illustrated in Fig. 14. Differences between the simulated and measured results are attributed to manufacturing inaccuracy.

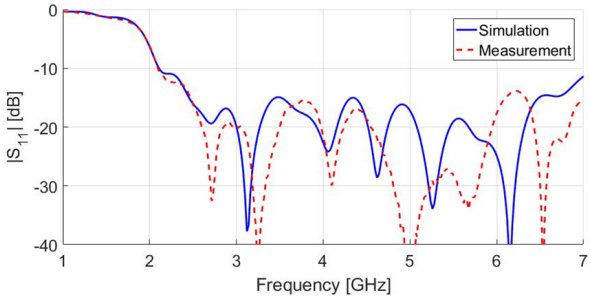

Fig. 14. Simulated and measured input reflection coefficient, S_{11}, of the BAVA in free-space.

We emphasize that, compared to the antenna presented in [39], which has a dimension of 44 mm but uses a dense embedding medium, our BAVA design is quite compact considering that it radiates in air. This proves that it is possible to have miniaturized antennas even in dry systems.

The antenna elements are intended to be positioned in a cylindrical configuration around the breast, as sketched in Fig. 1 by rotating the antenna around the breast. We lay the antennas horizontally to allow for more measurement planes along the z-direction.

C. Experimental setup

For the measurements, we fabricated an elevated styrofoam structure with the breast model placed at the center. The styrofoam material ($\epsilon_r \approx 1$) ensures that the structure does not influence the measurements. In addition, the height at which the breast model and the antenna are placed minimizes any influence from the floor. The measurement setup is shown in Fig. 15. It approximates the examination scenario, with the patient laying in the prone position and the breast pending from a cavity in the examination bed.

Fig. 15. Overview of the experimental setup.

Measurements were performed in the frequency-domain between 2 GHz and 5 GHz using a Vector Network Analyzer (VNA). A single BAVA element was connected to the VNA. The cylindrical antenna configuration is emulated by rotating

the breast phantom while keeping the antenna fixed. The diameter of the cylindrical antenna distribution is approximately 120 mm, corresponding approximately to average 17 mm distance to the breast wall.

The setup allows for continuous z-axis positioning of the antenna. We used 4 antenna heights, each one with 24 azimuth positions over the circumference. The upper height (i.e. closer to the chest) is at z = -13 mm and the subsequent ones are spaced with 10 mm steps. Note that according to our axes system, the breast is at negative z-values (Fig. 1).

VI. Breast Surface Reconstruction and Distance Estimation System

The exact antenna distance to the non-symmetric breast is needed for effective skin artifact removal and improved image retrieval from the inversion algorithm. Therefore, it is imperative to estimate the breast shape in a way that is simultaneously practical for a real exam.

The proposed system is based on a Logitech C930e webcam [50]. The camera, located in one side of the setup, takes 12 snapshots for different azimuth angles of the breast (between 0º and 165º), against a contrasting background. An example is shown in Fig. 16 (a).

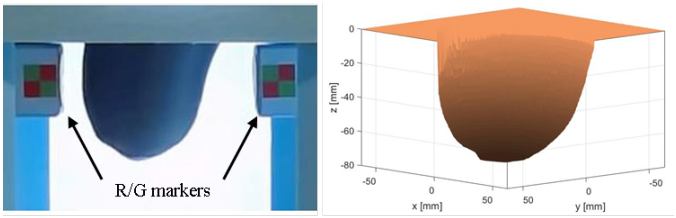

(a) (b)

Fig. 16. (a) Example of snapshot taken by the webcam; (b) Reconstructed breast surface using the proposed webcam system.

The distance scale is estimated by placing two Red/Green (R/G) markers at a known distance. We then apply a Template Matching Correlation Technique (TMCT) [51], to identify the markers in each snapshot. This technique is widely used in digital image processing for pattern finding, due to its simplicity, rapid execution, robustness [52], and resilience to brightness variations.

The process allows calculating 12 breast meridian profiles from 12 snapshots. This is a relatively straightforward process, based on breast edge detection against a background contrast and pixel counting. In our setup, the distance between breast and antenna varies from around 9 mm up to 30 mm. This variation is due solely to the non-symmetric shape of the breast, since the cylindrical antenna distribution has constant radius.

Two steps are used to obtain a full three-dimensional reconstruction of the breast shape from the determined 12 vertical profiles. First, we obtain an interpolation function for each meridian profile. This step is followed by another interpolation of the points from all profiles contained in each z-plane, in order to achieve a closed curve (the breast is approximately elliptical for constant z). By repeating this procedure for all z-planes with a desired resolution along this coordinate (0.5 mm in our case) we get the tridimensional surface of the breast. Fig. 16 (b) shows the final breast surface estimation of the anthropomorphic model used in the setup.

This process is simple, compatible with real-time processing and sufficiently accurate for MWI. Comparison between the reconstructed breast dimensions and the actual breast phantom size revealed a maximum error of about 2 mm. Moreover, it can be implemented using any commercial webcam.

VII. Experimental Results

Prior to imaging the breast we quantified the noise floor of our fully-featured setup to be around $-110dB$ (relative to an input power of 10 dBm), whereas the tumor response magnitude lies between –45 dB and –80 dB. The latter was calculated as $S_{11}^{cal} - S_{11}^{tmr}$, where S_{11}^{tmr} is the measured S_{11} in the presence of the breast with tumor and S_{11}^{cal} is the measured S_{11} in the presence of the healthy breast (i.e. without tumor). Thus, an increase in skin backscattering by as much as 8 dB, as concluded in section IV, is manageable and, therefore, does not preclude a dry imaging setup.

In order to fully assess the capability of the dry MWI system, we performed experimental tests with the tumor located at different positions in the breast volume, both for homogeneous and heterogeneous breasts. The artifact removal was applied considering N_n = 2 antennas, contained in the same height as the central antenna (the different antenna heights are considered independently). For each antenna position, we considered N_f = 34 frequency points in the 2-5 GHz interval.

In the first detection scenario, we considered the tumor at (x_t, y_t, z_t) = (15, -20, -32) mm immersed in homogeneous breast. This location is intentionally far enough from the breast walls, where the imaging resolution is expected to easily distinguish between the skin and the tumor. The imaging results from our system are shown in Fig. 17 in the main cuts. The white contours identify the limits of the breast and tumor.

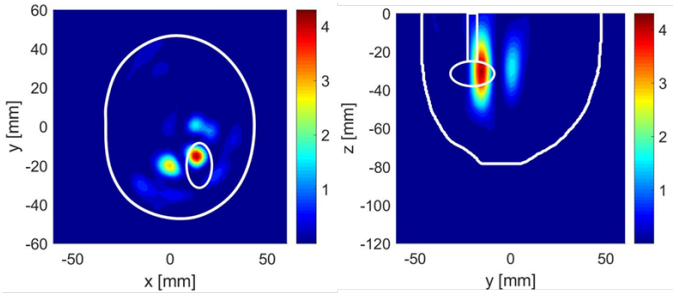

(a) (b)

Fig. 17. Imaging results of the homogeneous breast at (a) z = -30 mm and (b) x = 12 mm. The tumor is located at (15,-20,-32) mm. The white contours identify the limits of the breast and tumor.

We successfully detect the tumor in the correct position, with TCR = 1.5 dB and TMR = 14.4 dB. However, the tumor shape is elongated along the z-direction. Two reasons contribute to this result. Firstly, as mentioned, our cylindrical antenna distribution uses only four antenna heights, limited by the breast z-extent with reasonably vertical wall. As a result,

the achievable resolution along the z-direction is lower. This could be improved by adding more antenna rings, but at the expense of a more complex setup. Secondly, less important, the empty plastic tube used to fill the tumor cavity also presents some dielectric contrast relative to the background liquid, contributing to the backscattering.

In order to highlight the advantage of the proposed artifact removal algorithm, we compare it to state-of-the-art methods. We tested the artifact removal algorithms described in [30] and [36]. The first algorithm calculates the average of the S_{11} measured for the neighboring antenna positions and subtracts it from the S_{11} measured for the position of interest. As for [36], its algorithm weighs and combines the signals based on finite impulse response (FIR) filters, in an attempt to minimize the early portion of the time domain signal. The reconstructed images using these two algorithms are shown in Fig. 18.

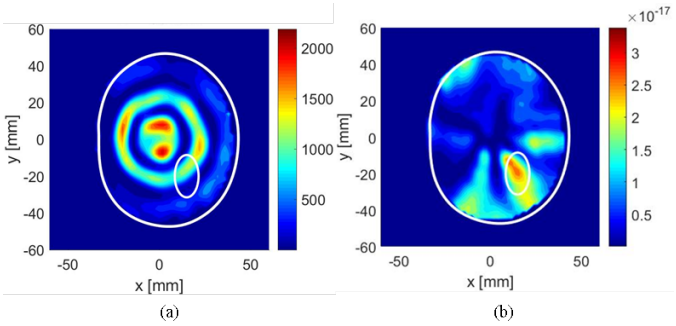

Fig. 18. Imaging results of the homogeneous breast (z = -30 mm) using skin artifact removal methods from the literature (a) neighborhood-based [30] and (b) FIR filter-based [36]. The tumor is located at (15,-20,-32) mm. The white contours identify the limits of the breast and tumor.

The tumor is clearly not detected in the first case, mainly because the algorithm is affected by the non-symmetric distance between the antennas and the breast surface. The FIR-based algorithm provides better results, but the clutter level is too high to distinguish the tumor from unwanted artifacts (TCR = 0.04 dB, TMR = 7.1 dB). This algorithm fails mostly because the skin reflection varies too much to be able to combine the signals and successfully remove the artifacts.

Due to space restrictions, the comparison of these methods is omitted for the next scenarios. Yet, we note that in all cases the alternative methods exhibit the same poor performance as in Fig. 18.

The second scenario is intended to demonstrate the capability of the artifact removal to preserve the response of the tumor when the distance from the latter to the skin is less than the theoretical resolution of the imaging system, Δd = 12.5 mm in the present case. This is a significant challenge for artifact removal algorithms, especially for those implementing time or spatial gating, which struggle to distinguish between two close scatterers. To this end, we have positioned the same tumor at (x_t, y_t, z_t) = (-20, -22, -32) mm. At these coordinates the tumor is estimated to be about 5 mm from the skin. The reconstructed reflectivity of the breast is presented in Fig. 19.

Again, the tumor is detected at the correct position, despite being closer to the skin than the theoretical image resolution. In this case we computed TCR = 4.1 dB showing very

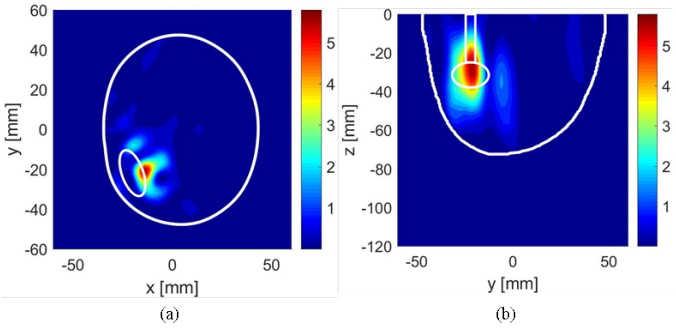

Fig. 19. Imaging results of the homogeneous breast at (a) z = -26 mm and (b) x = -14 mm. The tumor is located at (-20,-22,-32) mm, at 5 mm distance from the skin. The white contours identify the limits of the breast and tumor.

good detection results. These results demonstrate the artifact removal can handle tumors close to the skin.

Lastly, in the third scenario we evaluate the capability of the imaging system to detect tumors in heterogeneously dense breasts. To this end, we included the fibroglandular container (Fig. 11) filled with the corresponding liquid. The tumor was placed at (x_t, y_t, z_t) = (15, -25, -32) mm. Fig. 20 illustrates the imaging results obtained under these conditions.

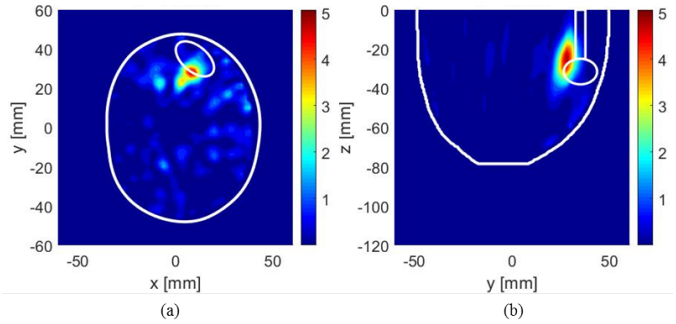

Fig. 20. Imaging results of the heterogeneous breast at (a) z = -24 mm and (b) x = 8 mm. The tumor is located at (10,35,-32) mm. The white contours identify the limits of the breast and tumor.

Even in low contrast scenarios, the tumor is correctly detected with TCR = 2.33 dB. However, the clutter level has increased due to the backscattering of the fibroglandular tissues, which resulted in TMR = 13.4 dB. Yet, the positioning error is just 10.8 mm, which we consider good for the intended primary screening technique.

The metrics calculated in the three discussed scenarios are summarized in Table III. Although tumor shape is not correctly reproduced, we stress that a sharp isolated detection clearly above the clutter is a much valuable result, as it gives a reliable indication of a diseased tissue, since it results from the known high contrast of unhealthy tissues.

We have performed additional experimental tests for other tumor positions (not shown here), and the obtained detection metrics were similar to the above.

VIII. Conclusion

We assessed the feasibility of a dry MWI setup, with the advantage of being contactless, more hygienic and potentially

TABLE III
CALCULATED IMAGING METRICS.

Figure		Fig. 17	Fig. 19	Fig. 20
(x_t, y_t, z_t)	Actual	(15,-20,-32)	(-20,-22,-32)	(10,35,-32)
	Detection	(14,-16,-30)	(-14,-22,-26)	(8,28,-24)
Breast composition		Homogeneous	Homogeneous	Heterogeneous
TCR [dB]		1.5	4.1	2.33
TMR [dB]		14.44	14.6	13.4
PE [mm]		4.6	8.5	10.8
NPE		0.37	0.68	0.86

more practical. To this end, we quantified the skin backscattering reduction when the breast is immersed in a matching media. In the best case scenario, we concluded that the reflection is mitigated by 8 dB for dense embedding medium of permittivity $\epsilon_r = 30$. We showed that this reduction is insufficient to rule out a dry imaging setup, given that the noise floor of imaging setups is sufficiently low, as to accommodate for the lower power reaching the tumor.

However, more robust artifact removal algorithm had to be developed not only to tackle the stronger skin artifacts, but also the additional challenge posed by the non-uniform shape of the pending breast. We proposed an adaptive artifact removal algorithm based on SVD. The method is robust and automation-compatible, allowing isolating the tumor response even when its distance to the skin is less than the theoretical spatial resolution of the system. This feature is enabled by the surface estimation method based on a webcam, which feeds the breast surface data to the imaging algorithms contributing to improve its performance.

Moreover, we designed a very compact broadband antenna with adequate performance despite not benefiting from a dense contact medium, in order to fit more antennas around the breast. All these elements were integrated in a demonstrator that included an anthropomorphic heterogeneous breast phantom. We obtained very good detection of the tumor in different positions, according to established quantitative metrics, despite the low contrast in the presence of fibroglandular tissue.

In summary, this work proved that a dry setup with proper signal processing is feasible for operation in real exams. It also showed that the setup can be compact and cost effective. In the future, we plan to improve imaging results using regularization techniques. We will explore the possibility of characterizing the antenna, in order to minimize the level of uncertainty in the linear observation model.

ACKNOWLEDGMENT

The authors acknowledge Carlos Brito and Jorge Farinha for prototype and experimental setup fabrication and also António Almeida for the measurements. In addition, the authors thank Prof. Nadine Joachimowicz and Prof. Bernard Duchêne for giving access to the GeePs-L2S breast phantom that we used in preparatory trials.

REFERENCES

[1] E. C. Fear, et al., "Confocal microwave imaging for breast cancer detection: localization of tumors in three dimensions," *IEEE Trans. Biomed. Eng.*, vol. 48, no. 8, pp. 812-822, Aug. 2002.

[2] F. Gao, et al., "Sensitivity of the distorted born iterative method to the initial guess in microwave breast imaging," *IEEE Trans. Antennas Propag.*, vol. 63, no. 8, pp. 3540-3547, Aug. 2015.

[3] T. M. Habashy, et al., "Beyond the Born and Rytov approximations: a nonlinear approach to electromagnetic scattering," *J. Geophys. Res.*, vol. 98, no. B2, pp. 1759–1775, Feb. 1993.

[4] J. D. Shea, et al., "Three-dimensional microwave imaging of realistic numerical breast phantoms via a multiple-frequency inverse scattering technique," *Med. Phys.*, vol. 37, no. 8, pp. 4210-4226, Aug. 2010.

[5] J. M. L. Sanchez, and J. F. Guash, "3-D radar imaging using range migration techniques," *IEEE Trans. Antennas Propag.*, vol. 48, no. 5, pp. 728-737, May 2000.

[6] A. Elahi, et al., "Hybrid artifact removal for confocal microwave breast imaging," *IEEE Antennas Wireless Propag. Lett.*, vol. 13, pp. 149-152, 2014.

[7] M. Klemm, et al., "Microwave radar-based breast cancer detection: imaging in inhomogeneous breast phantoms," *IEEE Antennas Wireless Propag. Lett.*, vol. 8, pp. 1349-1352, 2009.

[8] G. Ruvio, et al., "Breast cancer detection using interferometric MUSIC: experimental and numerical assessment," *Med. Phys.*, vol. 41, no. 10, pp. 1-11, Oct. 2014.

[9] D. Byrne, et al., "Compound radar approach for breast imaging," *IEEE Trans. Biomed. Eng.*, vol. 64, no. 1, pp. 40-51, Jan. 2017.

[10] M. Asefi , et al., "An experimental phantom study for air-based quasi-resonant microwave breast imaging," *IEEE Trans. Microw. Theory Techn.*, vol. -, no. -, pp. 1-9, April 2019.

[11] K. Nemez, et al., "Modeling error and calibration techniques for a faceted metallic chamber for magnetic field microwave imaging," *IEEE Trans. Microw. Theory Techn.*, vol. 65, no. 11, pp. 4347–4356, Nov. 2017.

[12] D. R. Herrera, et al., "Manufacture and testing of anthropomorphic 3D-printed breast phantoms using a microwave radar algorithm optimized for propagation speed," *2017 11th European Conference on Antennas and Propagation (EUCAP)*, pp. 3480-3484, Paris, France, March 2017.

[13] D. F. Tapia, et al., "A Singular value decomposition approach for microwave holography imaging of the breast: a feasibility study," *2016 10th European Conference on Antennas and Propagation (EuCAP)*, pp. 1-2, Davos, Switzerland, 2016.

[14] M. Lazebnik, et al., "A large-scale study of the ultrawideband microwave dielectric properties of normal, benign and malignant breast tissues obtained from cancer surgeries," *Phys. Med. Biol.*, vol. 52, no. 20, pp. 6093-6115, 2007.

[15] R. K. Amineh, et al., "Near-field microwave imaging based on aperture raster scanning with TEM horn antennas," *IEEE Trans. Antennas Propag.*, vol. 59, no. 3, pp. 928-940, Mar. 2011.

[16] T. C. Williams, et al., "Laser surface estimation for microwave breast imaging systems," *IEEE Trans. Biomed. Eng.*, vol. 58, no. 5, pp. 1193-1199, May 2011.

[17] D. W. Winters, et al., "Estimating the breast surface using UWB microwave monostatic backscatter measurements," *IEEE Trans. Biomed. Eng.*, vol. 55, no. 1, pp. 247-256, Jan. 2008.

[18] V. Klema, and A. Laub, "The singular value decomposition: Its computation and some applications," *IEEE Trans. Autom. Control*, vol. 25, no. 2, Apr. 1980.

[19] D. Li, et al., "Conformal microwave imaging for breast cancer detection," *IEEE Trans. Microw. Theory Tech.*, vol. 51, no. 4, pp. 1179–1186, Apr. 2003.

[20] G. Ruvio, et al., "Comparisn of noncoherent linear breast cancer detection algorithms applied to 2-D numerical model," *IEEE Antennas Wireless Propag. Let.*, vol. 12, pp. 853-853, 2013.

[21] N. K. Nikolova, "Microwave imaging for breast cancer," *IEEE Microw. Mag.*, vol. 12, no. 7, pp. 78-94, Dec. 2011.

[22] M. Klemm, et al., "Radar-based breast cancer detection using a hemispherical antenna array – experimental results," *IEEE Trans. Antennas Propag.*, vol. 57, no. 6, pp. 1692-1704, June 2009.

[23] A. Santorelli, et al., "Image classification for a time-domain microwave radar system: experiments with stable modular breast phantoms," *2015 9th European Conference on Antennas and Propagation (EuCAP)*, pp. 1-5, Lisbon, Portugal, April 2015.

[24] M. Jalilvand, et al., "Ultra wideband compact near-field imaging system for breast cancer detection," *IET Microw. Antennas Propag.*, vol. 9, no. 10, pp. 1009-1014, 2015.

[25] M Bertero, and P. Boccaci, *Introduction to inverse problems in imaging*, Institute of Physics, Jan. 1998.

[26] C. Curtis, et al., "An analysis of the assumptions inherent to near-field beamforming for biomedical applications," *IEEE Trans. Comput. Imaging*, vol. 3, no. 4, pp. 953-965, Dec. 2017.

[27] Declan O'Loughlin, et al., "Parameter search algorithms for microwave radar-based breast imaging: focal quality metrics as fitness functions," *Sensors*, vol. 17, no. 12, Dec. 2017, Art. no. 2823.

[28] J. M. Felício, et al., "Antenna design and near-field characterization for medical microwave imaging applications," *IEEE Trans. Antennas Propag.*, vol. -, no. -, pp. 1-14, Mar. 2019.

[29] G. H. Hardy, W. W. Rogosinski, *Fourier Series*, Dover Publications Inc., United States of America, 1999.

[30] B. Maklad, et al., "Neighborhood-based algorithm to facilitate the reduction of skin reflections in radar-based microwave imaging," *Prog. Electromagn. Res.*, vol. 39, pp. 115-139, 2012.

[31] C. Eckart, and G. Young, "The approximation of one matrix by another of lower rank," *Psychometrika*, vol. 1, no. 3, pp. 211-218, Sep. 1936.

[32] M. Soumekh, *Synthetic aperture radar signal processing with MATLAB algorithms*, New York: John Wiley & Sons, Inc., 1999.

[33] (April 2018). CST – Computer Simulation Technology [Online]. Available: https://www.cst.com/.

[34] C. Balanis, *Antenna theory: analysis and design*, Harper & Row, Publishers, Inc., 1982.

[35] A. B. Carlson, et al., *Communication Systems: an introduction to signals and noise in electrical communication*, McGraw Hill, Fourth edition, 2002.

[36] E. J. Bond, et al., "Microwave imaging via space-time beamforming for early detection of breast cancer," *IEEE Trans. Antennas Propag.*, vol. 51, no. 8, pp. 1690-1705, Aug. 2003.

[37] I. Catapano, et al., "On quantitative microwave tomography of female breast," *Prog. Electromagn. Res.*, vol. 97, pp. 75-93, 2009.

[38] S. I. Latif, et al., "A directional antenna in a matching liquid for microwave radar imaging," *Int. J. Antennas Propag.*, vol. 2015, pp. 1-8, 2015.

[39] J. Bourqui, et al., "Balanced antipodal vivaldi antenna with dielectric director for near-field microwave imaging," *IEEE Trans. Antennas Propag.*, vol. 58, no. 7, pp. 2318-2326, July 2010.

[40] S. Gabriel, et al., "The dielectric properties of biological tissues: III. parametric models for the dielectric spectrum tissues," *Phys. Med. Biol.*, vol. 41, no. 11, pp. 2271–2293, 1996.

[41] S. J. Orfanidis, *Electromagnetic Waves and Antennas*, Rutgers University, ch. 5, 2008.

[42] J. T. L. Pope, et al., "Breast skin thickness: normal range and causes of thickening shown on film-screen mammography," *J. Can. Assoc. Radiol.*, vol. 35, no. 4, pp. 365–368, 1984.

[43] J. M. Felício, et al., "Complex permittivity and anisotropy measurement of 3D-printed PLA at microwaves and millimeter-waves," *International Conference on Applied Electromagnetics and Communications (ICECOM 2016)*, pp. 1-6, Dubrovnik, Croatia, Sep. 2016.

[44] M. J. Burfeindt, et al., "MRI-derived 3-D-printed breast phantom for microwave breast imaging validation," *IEEE Antennas Wireless Propag. Lett.*, vol. 11, pp. 1610-1613, 2012.

[45] (April 2018) "Ultimaker", [Online]. Available: https://ultimaker.com/.

[46] N. Joachimowicz, et al., "Breast phantoms for microwave imaging," *IEEE Antennas Wireless Propag. Lett.*, vol. 13, pp. 1333-1336, 2014.

[47] A. Kiourti, et al., "Miniature implantable antennas for biomedical telemetry: from simulation to realization," *IEEE Trans. Biomed. Eng.*, vol. 59, no. 11, pp. 3140-3147, Nov. 2012.

[48] J. Langley, et al., "Novel ultrawide-bandwidth Vivaldi antenna with low crosspolarisation," *Electron. Lett.*, vol. 29, no. 23, pp. 2004-2005, Nov. 1993.

[49] K. Kikuta, and A. Hirose, "Compact Folded-Fin Tapered Slot Antenna for UWB Applications," *IEEE Antennas Wireless Propag. Lett.*, vol. 14, pp. 1192-1195, 2015.

[50] (June 2017). Logitech [Online], Available: http://www.logitech.com/.

[51] A. K. Jain, "Statistical pattern recognition: a review," *IEEE Trans. Pattern Anal. Mach. Intell.*, vol. 22, no. 1, pp. 4-37, Jan 2000.

[52] J. P. Lewis, "Fast normalized cross-correlation," *Vis. Interface*, vol. 10, no. 1, pp. 120–123, May 1995.

João M. Felício (S'14) was born in Lisbon, Portugal, in 1990. He received the MSc and PhD degrees in Electrical and Computer Engineering from the Instituto Superior Técnico (IST), University of Lisbon, Lisbon, in 2014 and 2018, respectively. He is currently a Researcher with the Instituto de Telecomunicações, Lisbon. He is also an Invited Professor with the Departamento de Ciências e Tecnologias da Informação, Instituto Universitário de Lisboa (ISCTE-IUL), Lisbon.

His main interests include microwave imaging, antenna design, and antennas for biomedical applications.

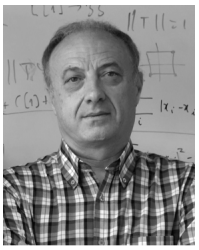

José M. Bioucas-Dias (S'87–M'95–SM'15–F'17) received the EE, MSc, PhD, and Habilitation degrees in electrical and computer engineering from Instituto Superior Técnico (IST), Universidade Técnica de Lisboa (now Universidade de Lisboa), Portugal, in 1985, 1991, 1995, and 2007, respectively. Since 1995, he has been with the Department of Electrical and Computer Engineering, IST, where he is a Professor and teaches inverse problems in imaging and electric communications. He is also a Senior Researcher with the Pattern and Image Analysis group of the Instituto de Telecomunicações, which is a private non-profit research institution.

His research interests include inverse problems, signal and image processing, pattern recognition, optimization, and remote sensing. He has introduced scientific contributions in the areas of imaging inverse problems, statistical image processing, optimization, phase estimation, phase unwrapping, and in various imaging applications, such as hyperspectral and radar imaging. He was included in Thomson Reuters' Highly Cited Researchers 2015 list and received the IEEE GRSS David Landgrebe Award for 2017.

Jorge R. Costa (S'97–M'03–SM'09) was born in Lisbon, Portugal, in 1974. He received the Licenciado and Ph.D. degrees in electrical and computer engineering from the Instituto Superior Técnico, Technical University of Lisbon, Lisbon, in 1997 and 2002, respectively. He is currently a Researcher with the Instituto de Telecomunicações, Lisbon. He is also an Associate Professor with the Departamento de Ciências e Tecnologias da Informação, Instituto Universitário de Lisboa (ISCTE-IUL), Lisbon. He is the Co-Author of four patent applications and over 150 contributions to peer-reviewed journals and international conference proceedings. More than 30 of these papers have appeared in IEEE journals. His current research interests include lenses, reconfigurable antennas, MEMS switches, UWB, MIMO, and RFID antennas. Dr. Costa was the Co-Chair of the Technical Program Committee of the European Conference on Antennas and Propagation (EuCAP 2015), Lisbon, and the General Vice-Chair of EuCAP 2017, Paris. He was a Guest Editor of the Special Issue on Antennas and Propagation at mm- and Sub mmWaves, from the IEEE TRANSACTIONS ON ANTENNAS AND PROPAGATION, in 2013. He served as an Associate Editor of the IEEE TRANSACTIONS ON ANTENNAS AND PROPAGATION from 2010 to 2016.

Carlos A. Fernandes (S'86–M'89–SM'08) received the Licenciado, MSc, and PhD degrees in Electrical and Computer Engineering from Instituto Superior Técnico (IST), Technical University of Lisbon, Lisbon, Portugal, in 1980, 1985, and 1990, respectively. He joined IST in 1980, where he is presently Full Professor at the Department of Electrical and Computer Engineering in the areas of microwaves, radio wave propagation and antennas. He is a senior researcher at the Instituto de Telecomunicações and member of the Board of Directors. He has co-authored a book, 2 book chapters, more than 200 technical papers in peer reviewed international journals and conference proceedings and 7 patents in the areas of antennas and radiowave propagation modeling. His current research interests include dielectric antennas for millimeter wave applications, antennas and propagation modeling for personal communication systems, RFID and UWB antennas, artificial dielectrics and metamaterials. He was a Guest Editor of the Special Issue on "Antennas and Propagation at mm- and Sub mm-Waves", from the IEEE Transactions on Antennas and Propagation, April 2013.